ACS APPLIED MATERIALS & INTERFACES

Research Article

www.acsami.org

High Rate Capability of Hydrogen Annealed Iron Oxide–Single Walled Carbon Nanotube Hybrid Films for Lithium-Ion Batteries

Zeyuan Cao and Bingqing Wei*

Department of Mechanical Engineering, University of Delaware, Newark, Delaware 19716, United States

Supporting Information

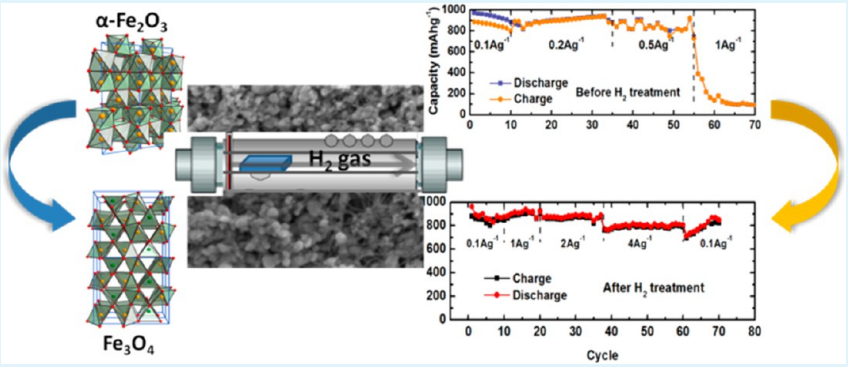

ABSTRACT: A facile and effective hydrogen annealing method has been demonstrated to synthesize iron oxide/SWNT hybrid films involving the thermal reduction of rhombohedral Fe_2O_3 to cubic Fe_3O_4 through the phase transformation while maintaining the morphological integrity of the films. The poor rate capability and cyclic stability of the original α-Fe_2O_3/SWNT hybrid films have been significantly improved by H_2 annealing. The prepared iron oxide/SWNT hybrid films have a high capacity of 786 mA h g^{-1} at a high current density of 4 A g^{-1} with a prolonged lifetime. The enhancement of the electrochemical performance is attributed to the presence of highly conductive Fe_3O_4, accelerated charge-transfer kinetics, and the increased Li^+ diffusivity confirmed by electrochemical impedance spectra and galvanostatic intermittent titration.

KEYWORDS: *hydrogen annealing, iron oxides, single-walled carbon nantube, hybrid films, lithium-ion batteries, electrochemical kinetics*

INTRODUCTION

Transition metal oxides (Co_3O_4,[1] TiO_2,[2] etc.) have been intensively studied as alternative anodes to graphitic carbons for application in lithium ion batteries because of their ultrahigh specific capacity (as high as 1000 $mAhg^{-1}$, approximately three times that of graphite with 372 mA h g^{-1}).[3,4] The high capacities result from the conversion reactions of $Li + M_xO_y \leftrightarrow M^0 + Li_2O$ instead of the intercalation mechanism of Li ions into interstitial sites.[3] Among these oxides, iron oxides including Fe_2O_3 and Fe_3O_4 are considered as particularly promising electrode materials due to their natural abundance, low cost, environmental benignity, low toxicity, and high capacity.[5,6] It has been demonstrated that maximum theoretical capacities beyond 1000 mA h g^{-1} are able to be achieved as up to 6 and 8 mol of Li ions can be accommodated by Fe_2O_3 and Fe_3O_4, respectively.[7,8]

However, the low rate capabilities governed by the slow kinetics of Li-ion diffusion and the poor conductivity of the $M_xO_y/M^0/Li_2O$ matrix still remain challenges even with the use of nanostructured materials to reduce the diffusion length, as well as high conductive additives, e.g., single-walled carbon nanotubes (SWNTs), to maintain electrical and mechanical contact with the current collectors.[3,9] In our previous work,[9] hametite α-Fe_2O_3 nanoparticle/SWNT hybrid films have been successfully synthesized to promote an excellent active material/current collector contact by means of a simple heat treatment method. Despite the high capacity, the rate performance of such hybrid-film anodes at over 1 A g^{-1} is unsatisfactory. To overcome this drawback and further improve their electrochemical performance, we have adopted a strategy of annealing in a reductive or inert atmosphere based on the two following facts:

First, annealing in an inert gas could induce surface defects of lower-state metallic ions and oxygen vacancies of the oxides.[10] The Li-ion insertion/extraction process could be facilitated due to the improved charge-transfer conductivity and modified surface thermodynamics with the presence of defects.[10] Meanwhile, the preservation of the integrity in the morphology of electrodes enables sustained rechargeability.[10]

Second, the thermal treatment in a reductive gas, for example, H_2, has been demonstrated to partially reduce the Fe^{3+} in α-Fe_2O_3 to Fe^{2+} in Fe_3O_4.[11] The hopping between Fe^{3+}

Received: July 25, 2013
Accepted: September 17, 2013
Published: September 17, 2013

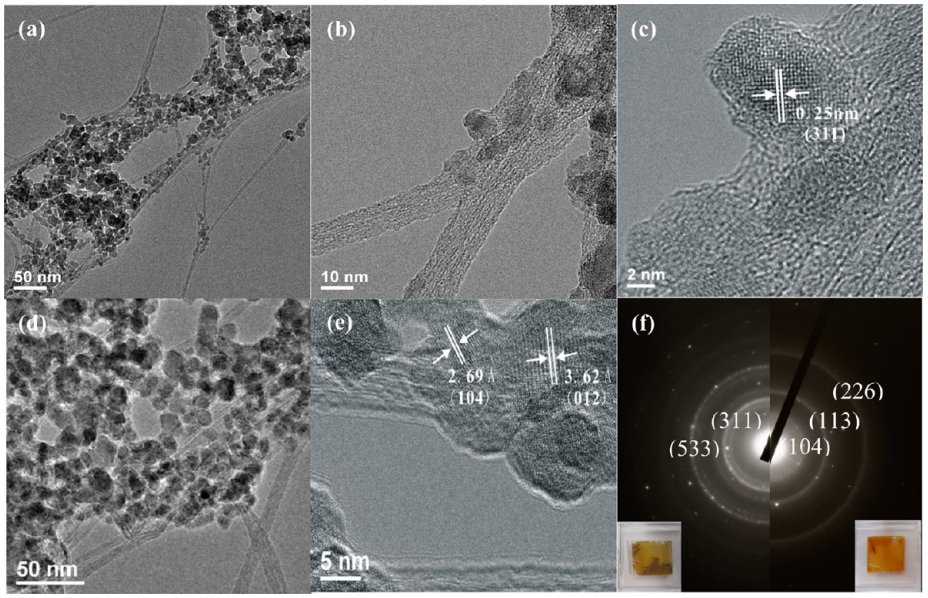

Figure 1. (a, b) TEM images of iron oxide/SWNT hybrid films after H_2 annealing; (c) HRTEM image of Fe_3O_4 nanocrystal in the hybrid films after H_2 annealing; (d) TEM image of α-Fe_2O_3/SWNT hybrid films before H_2 annealing; (e) HRTEM image of α-Fe_2O_3 nanocrystals in the hybrid films before H_2 annealing; (f) SAED patterns of the hybrid films before (right) and after (left) H_2 annealing with the corresponding photographs inset in red and brownish on the same side.

and Fe^{2+} at the octahedral sites in the cubic inverse spinel structure of Fe_3O_4 at room temperature renders it a half-metallic class with a high electronic conductivity (200 S/cm), which is only 1 order of magnitude lower than the minimum conductivity of a metal.[12]

Thus, herein we realize a partial conversion of Fe_2O_3/SWNT to Fe_3O_4/SWNT hybrid films by H_2 thermal reduction. As expected, the iron oxide/SWNT hybrid-film electrodes after H_2 annealing significantly enhance the rate capability and the cyclic stability for rechargeable lithium ion batteries. The reduced internal resistance and increased diffusivity of Li ions contribute to the improvement of their electrochemical performance.

EXPERIMENTAL SECTION

Synthesis of Iron Oxide (Fe_2O_3 and Fe_3O_4)/SWNT Hybrid Films. First, α-Fe_2O_3/SWNT macro-films were synthesized by a simple heat treatment on the SWNT macro-films, which were prepared using a modified floating chemical vapor deposition (CVD) method according to previously published work.[13] In brief, the precursor, a mixture of ferrocene and sulfur (atomic ratio Fe:S = 1:10, both from Sigma Aldrich), was heated to 1100−1150 °C in the tube furnace with a mixed-gas flow of Ar (1500 mL min^{-1}) and H_2 (150 mL min^{-1}) for 10−30 min. After being cooled down, the Fe-containing SWNT (Fe/SWNT) macro-films were obtained. Next, a simple heat treatment at 450 °C for 30 min in air was carried out on the as-prepared Fe/SWNT macro-films to obtain the α-Fe_2O_3/SWNT hybrid films. Lastly, the obtained α-Fe_2O_3/SWNT hybrid films were annealed at 360 °C for 2 h in H_2 atmosphere to be partially reduced to the iron oxide (Fe_3O_4 and Fe_2O_3)/SWNT hybrid films.

Characterization. The morphology and structure of the iron oxide/SWNT hybrid films were characterized by means of scanning electron microscopy (SEM mode, 3 kV, Zeiss Auriga 60 FIB/SEM) and transmission electron microscopy (TEM, JEOL JEM-2010F). X-ray diffraction (XRD) patterns were recorded within a 2θ range of 10 to 80° at 0.08°/step and 20s/step by Philips X'Pert diffractometer with Cu Kα radiation. Rietveld fitting was performed using the GSAS and EXPGUI package to identify the crystalline lattice parameters of iron oxides and quantitatively calculate the mass ratio of Fe_2O_3 and Fe_3O_4.[14] Raman spectroscopy (Bruker SENTERRA with 785 nm laser excitation) was employed to verify the crystalline structure of the iron oxides. X-ray photoelectron spectroscopy (XPS) was conducted on the EA 125 spectrometer with a nonchromatic Al Kα source (1486.5 eV). Thermogravimetric analysis (TGA) was carried out on a high resolution TGA instrument (Mettler-Toledo, SDA851e) from 0 to 1000 °C at a heating rate of 10 °C/min in flowing air. The thickness of iron oxides/SWNT hybrid films was measured by optical interferometer (WYKO NT9100, Veeco instrument Inc.)

Electrochemical Measurements. The electrodes were prepared by transferring the hybrid films onto the copper foil (9 μm thick) current collectors with the aid of several drops of ethanol to enable a solid adhesion, and then punching the Cu-supported films to disc with the diameter of 1/2 in. after they were dried in air. The mass of the hybrid films covering the disc-shaped electrodes was acquired from deducting the weight of bare Cu substrates using a micro/ultramicro balance (Mettler Toledo XP6) with 0.001 mg accuracy. The whole mass of the films are 0.25 mg by weight. CR2032 coin cells were assembled in an argon-filled glovebox (MBRAUN UNIlab). A coin cell consists of the hybrid film as the working electrode, a Celgard 2500 as the separator, and a lithium ribbon (0.38 mm thick, 99.9%, Sigma Aldrich) as the counter electrode in the 1 M $LiPF_6$ dissolved in 1:1 v/v ethylene carbonate (EC): diethyl carbonate (DEC) as electrolyte (Ferro Co.). The galvanostatic discharge−charge tests and galvanostatic intermittent titration technique (GITT) were carried out on BT-4 4-channel battery testing equipment (Arbin Instrument, ltd.). A series of current steps at 50 mA g^{-1} (~0.05C) for 1 h, each followed by a 12 h resting process comprised the GITT measurements between 0 and 3 V. The relaxation time of 12 h was to allow a full relaxation of lithium diffusion to reach

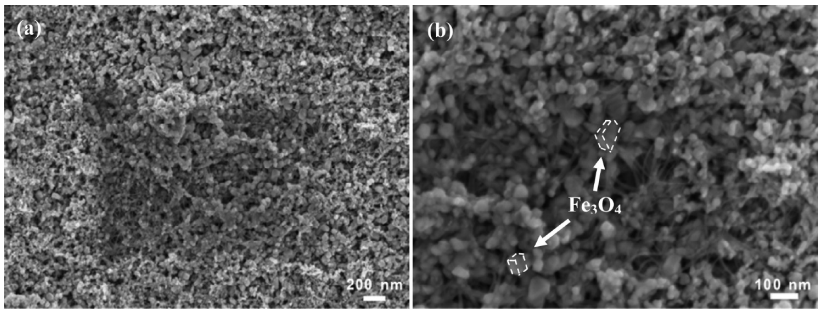

Figure 2. (a) SEM images of the iron oxide/SWNT hybrid films after H_2 annealing and (b) in a higher magnification.

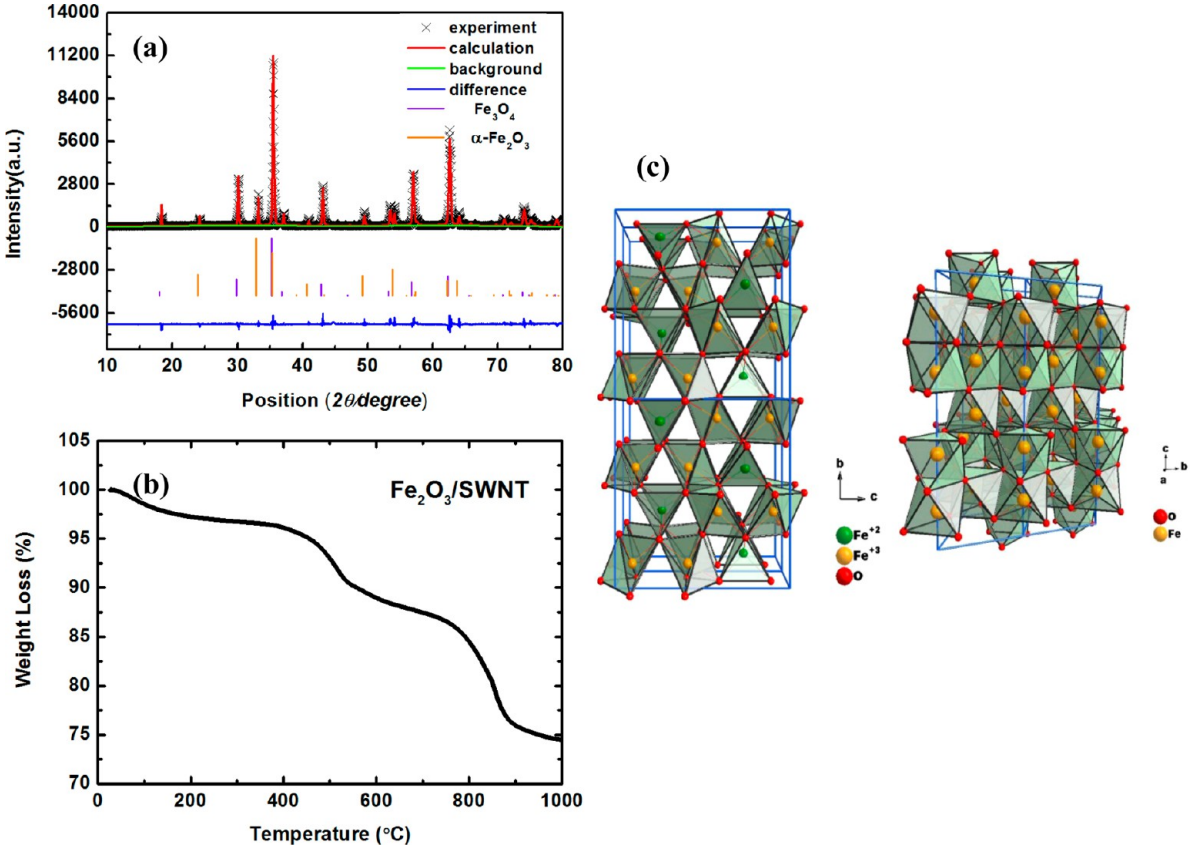

Figure 3. (a) XRD patterns and Rietveld fitting results of the iron oxide/SWNT hybrid films after H_2 annealing; (b) TGA curve of α-Fe_2O_3/SWNT hybrid films before H_2 annealing; (c) crystalline structure models of cubic Fe_3O_4 (left) and rhombohedral Fe_2O_3 (right).

equilibrium potential and to minimize self-discharge during the test. Electrochemical impedance spectroscopy (EIS) was performed by PARSTAT 2273 potentiostat/galvanostat (Princeton Applied Research) with a 10 mV amplitude of AC signal from 100 kHz to 10 mHz.

RESULTS AND DISCUSSION

TEM images of iron oxide/SWNT hybrid films after H_2 annealing (Figure 1a, b) and the α-Fe_2O_3/SWNT hybrid films before H_2 annealing (Figure 1d) all present a heterogeneous morphology of iron oxide nanocrystals with similar sizes (<20 nm) distributed on the entangled SWNT bundles. It is evident that the morphology of these nanocrystals is well maintained during the H_2 thermal reduction. SEM images (Figure 2) also demonstrate the retention of morphology with a uniform distribution of nanocrystals except for the typical cubic shape of Fe_3O_4 particles, which have a slightly more expanded volume than Fe_2O_3. This superfacially indicates the structure change during reduction but more evidence is needed from the following characterizations.

The high-resolution TEM (HRTEM) images in Figures 1c and 1e show the detailed crystalline structure of the iron oxide nanocrystals in the hybrid films after and before H_2 annealing, respectively. The well-defined lattice fringe spacing of 0.25 nm highlighted in Figure 1c is consistent with the interplanar spacing of (311) planes for Fe_3O_4, whereas that of 2.69 and 3.62 Å in Figure 1e correspond to the (104) and (012) planes of α-Fe_2O_3. The selected-area electron diffraction (SAED) patterns in Figure 1f also reveal two different well-resolved polycrystalline rings, which imply the conversion from hexagonal close-packed (hcp) structure of hametite α-Fe_2O_3 with the corresponding (104), (113), and (226) typical planes to the cubic close-packed (ccp) Fe_3O_4 with the corresponding (533) and (311) planes during the H_2 thermal reduction. The

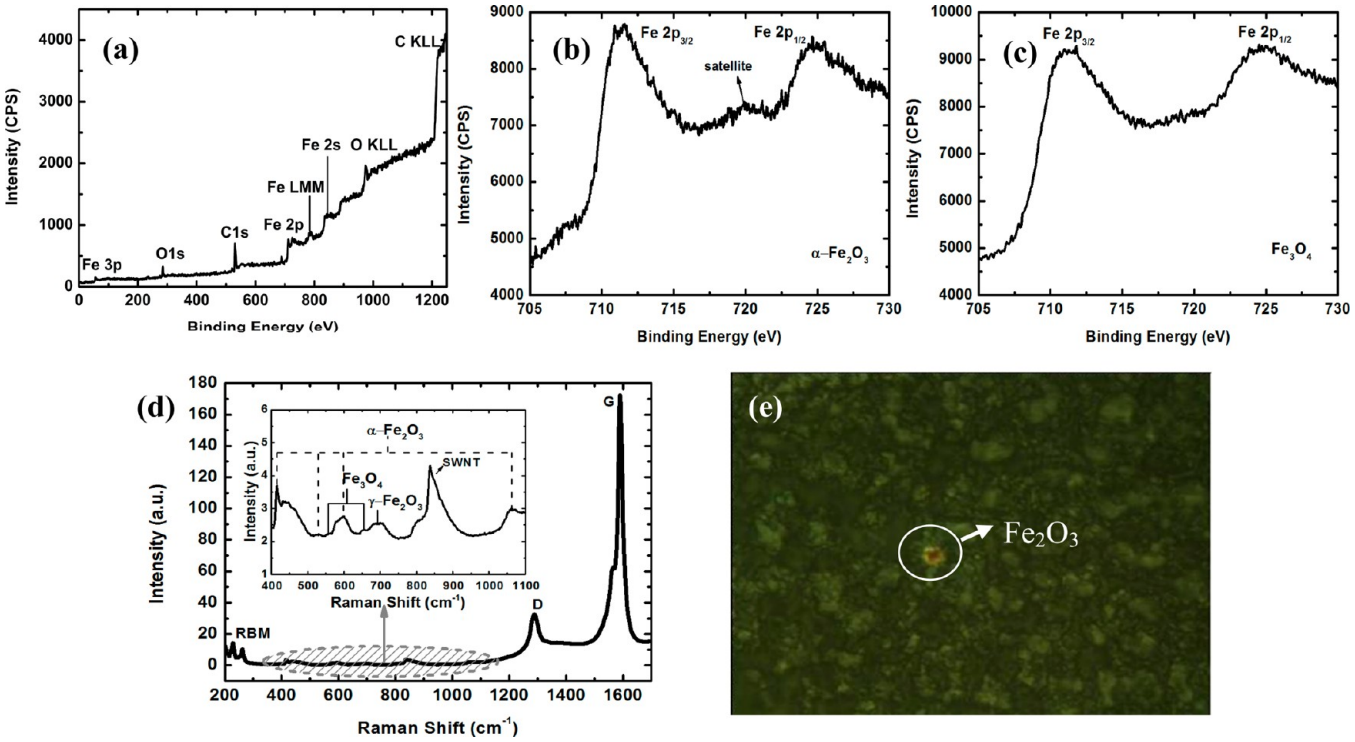

Figure 4. (a) XPS survey spectrum of the hybrid films; (b) XPS spectrum of Fe 2p for the hybrid films before H_2 annealing. The presence of the satellite peak of Fe $2p_{3/2}$ is the characteristics of the α-Fe_2O_3; (c) XPS spectrum of Fe 2p for the hybrid films after H_2 annealing. The absence of the satellite peak confirms the reduction of Fe_2O_3 to Fe_3O_4 after H_2 annealing. (d) Raman spectrum of the iron oxide/SWNT hybrid films after H_2 annealing, the inset illustrates the details of the spectrum from 400 to 1100 cm^{-1}; (e) the optical image snapshot showing the Fe_3O_4 was reoxidized to Fe_2O_3 as marked on the red spot.

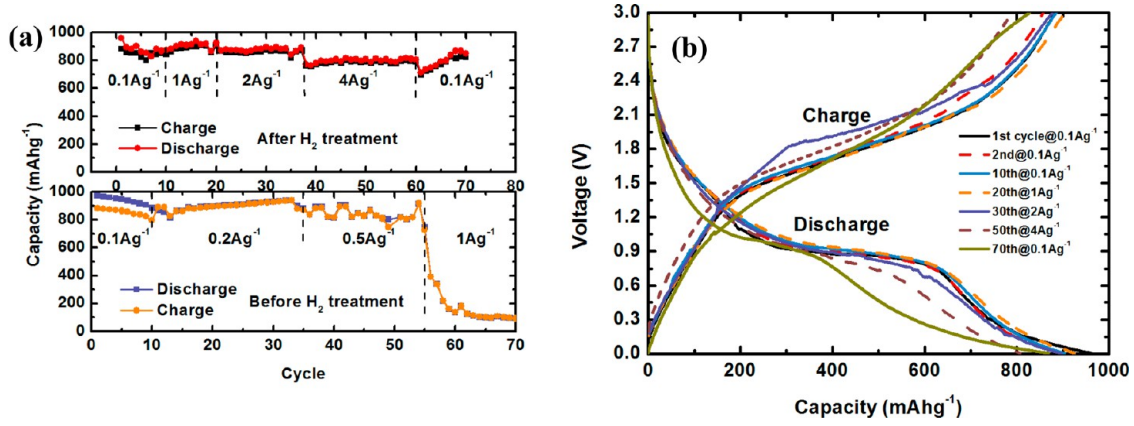

Figure 5. (a) Rate capabilities of the iron oxide/SWNT hybrid films after (top) and before (bottom) H_2 annealing; (b) discharge/charge profiles for the hybrid films after H_2 annealing corresponding to the selected cycles at various rates.

conversion can also be visibly reflected on the observation of the films' color change from red (right inset photography in Figure 1f) before H_2 annealing to brownish (left inset photography in Figure 1f) after H_2 annealing.

From the XRD pattern (Figure 3a) for the iron oxide/SWNT hybrid films after H_2 annealing, we can assess the reduction degree of the initially pure α-Fe_2O_3 and extract the detailed composition of the hybrid films. All the diffraction peaks could be indexed to two phases: the rhombohedral phase (Phase I) of α-Fe_2O_3 in $R\bar{3}c$ space group (JCPDS No.01−087−1164) and the cubic phase (Phase II) of Fe_3O_4 in $Fd\bar{3}m$ space group (JCPDS No.01−075−0033). The coexistence of Fe_3O_4 and Fe_2O_3 is in good agreement with the HRTEM results. The transformation from phase I to II involves the slip of atom-packed planes from AB to ABC stacking. Refinement was further applied to the XRD data by using the Rietveld fitting method to obtain the lattice parameters of the two phases: for α-Fe_2O_3, $a = b = 5.031705$ Å, $c = 13.743799$ Å, and $\alpha = \beta = 90°$, $\gamma = 120°$; for Fe_3O_4, $a = b = c = 8.387474$ Å and $\alpha = \beta = \gamma = 90°$, as depicted in their respective schematic crystal units (Figure 3c). The phase weight fraction of the two iron oxides was also quantitatively yielded: Fe_2O_3:Fe_3O_4 = 7.5%:92.5% for iron oxides, which constitute 75% of the hybrid films evaluated by TGA curve as shown in Figure 3b. The mean thickness of iron oxides/SWNT hybrid films is about 480 nm as shown in Figure S1 (Supporting Information).

XPS results presented in Figure 4a−e confirm the conversion between α-Fe_2O_3 and Fe_3O_4. In the survey spectrum (Figure

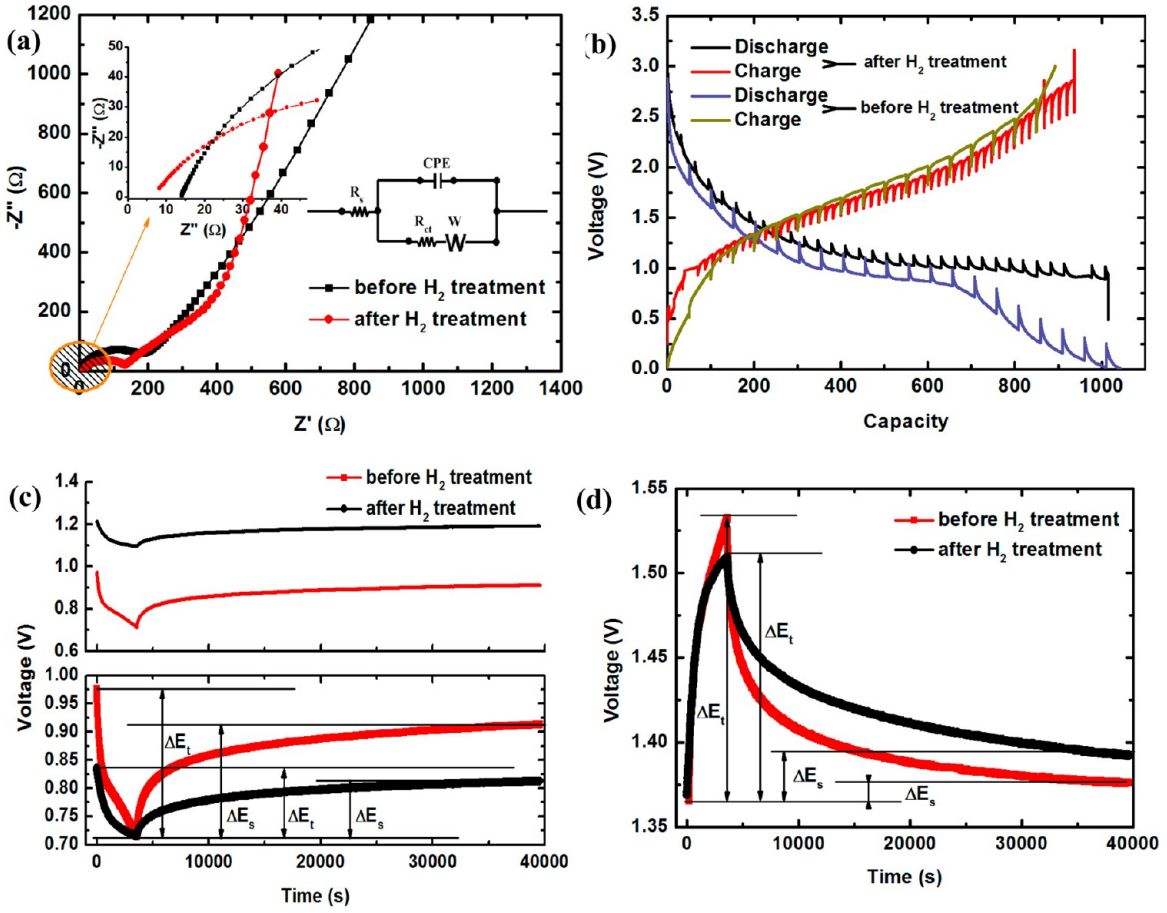

Figure 6. (a) Nyquist plots of the iron oxide/SWNT hybrid films before (red line) and after (black line) H_2 annealing with the inset equivalent circuit used for fitting; (b) GITT discharge/charge curves for the two hybrid films distinguished by different colors in the plot; (c) polarization curves at the plateau potential during charge processes for the two hybrid films; (d) polarization curves at the plateau potential during discharge processes for the two hybrid films.

4a), only the peaks assigned to three elements of Fe (2s, 2p, 3p, and LMM), O (1s and KLL) in the iron oxide states, and C (1s and KLL) coming from SWNTs were collected by detectors. For the α-Fe_2O_3/SWNT hybrid films before H_2 annealing in Figure 4b, the peaks at 711.45 and 725.1 eV are attributed to Fe $2p_{3/2}$ and Fe $2p_{1/2}$. The distinguishable peak at 719.9 eV is the satellite peak of Fe $2p_{3/2}$, which is typical for Fe_2O_3.[15] As it was previously reported that there was no satellite peak for Fe $2p_{3/2}$ of Fe_3O_4,[15] the absence of the satellite peak in Figure 4c for the iron oxide/SWNT hybrid films after H_2 annealing indicates the reduction of Fe_2O_3 to Fe_3O_4, where only the Fe $2p_{3/2}$ peak at 711.25 eV and the Fe $2p_{1/2}$ peak at 724.95 eV are present.

Raman spectrum (Figure 4d) of the iron oxide/SWNT hybrid films after H_2 treatment also exhibits the mixed bands ranging from 400 to 1100 cm^{-1} corresponding to Fe_2O_3 and Fe_3O_4 nanocrystals, whereas SWNTs show the D band at around 1300 cm^{-1}, G band at around 1600 cm^{-1}, and the radial breathing mode (RBM) in the range of 200−300 cm^{-1}, similar to the data in the literature.[16−18] The noticeable red spot marked in the image snapshot (Figure 4e) by optical microscopy attached with Raman is a reverse phase transformation of black Fe_3O_4 to be reoxidized to Fe_2O_3 in red color caused by the accumulating heat of laser with a power of 10 mV. This provides another reliable proof of the phase transformation from Fe_2O_3 to Fe_3O_4 because of the H_2 reduction.

The electrochemical performance of the iron oxide/SWNT hybrid films after H_2 treatment was then investigated. The comparison of the rate capabilities for the two samples before and after H_2 treatment was performed by the continuous discharge/charge cycling measurements at a variety of current densities from 0.1 A g^{-1} up to 4 A g^{-1}. Figure 5a shows that the initial specific discharge capacity is 960 mA h g^{-1} for the sample after H_2 treatment (represented as "film AH" for the following use) at the constant current density of 0.1 A g^{-1}. Although this highest value starts to drop due to the irreversible capacity resulting from the formation of the solid electrolyte interface between electrolyte and anode, the average capacity of this sample is as high as 847 mA h g^{-1} in the first 10 cycles at 0.1 A g^{-1}. The film AH also exhibits the excellent high-rate performance during the following cycling tests: the mean discharge capacities are 890 and 861 mA h g^{-1} corresponding to the cycles at 1 and 2 A g^{-1}. When the current density as high as 4 A g^{-1} is applied, the capacity still stabilizes at 786 mA h g^{-1} on average from the 40th to 60th cycle. It is also noted that for the last 10 cycles with the rate returning to the low current density of 0.1 A g^{-1}, the capacity gradually increass and retains 785 mA h g^{-1}, which is 93% of that for the initial 10 cycles at the same current density. On the contrary, the α-Fe_2O_3/SWNT hybrid films before H_2 annealing ("film BH") only exhibit a comparable specific capacity above 800 mA h g^{-1} to the film AH at the extremely low current densities of 0.1 and 0.2 A g^{-1}. The capacity of film BH fluctuates and fades quickly below 100

mA h g^{-1} when the current density is raised beyond 0.5 A g^{-1}. The facilitated fading at higher current density up to 1 A/g implies the slow kinetics and diffusivity become more critical in limiting the performance of the films. Meanwhile, the accumulated large volume change induced by lithiation/delithiation in all the previous cycles may result in the dissociation of iron oxides from the entanglement of SWNTs where only the relatively weak interaction force between them, aggravating the fast fading of capacity. The comparison data evidently indicate the improvement of the rate capability by H_2 annealing, suggesting that the kinetic property of lithium-ion insertion/extraction could be enhanced by H_2 annealing. In addition, the Coulombic efficiency in the initial 10 cycles at 0.1 A g^{-1} for film BH is also lower with a remarkably larger gap between discharge and charge capacity than that of film AH. This is probably attributed to the lower conductivity of Fe_2O_3 compared to that of Fe_3O_4.

The discharge/charge curves for film AH at different current densities in Figure 5b show a common behavior of conversion reaction with a similarly well-defined potential plateau at around 1 V versus Li^+/Li, corresponding to the phase reduction process of iron oxides (Fe_2O_3 and Fe_3O_4) into the Fe^0/Li_2O matrix. The well-overlapped curves before the 50th cycle with variation in the applied rates also reveal the excellent reversibility of the lithiation and delithiation processes. In contrast, it is worth noting that during the last several cycles when the rate is lowered to 0.1 A g^{-1}, the plateau length of the 70th-cycle discharge/charge profile, for example, becomes shortened, implying the retarded reduction of the iron oxides which results in the capacity deterioration. However, the additional capacity following the phase reduction process is in an increasing trend as described in Figure 5a. This is due to the full relaxation of lithium ion diffusion in the $Fe_3O_4/Fe^0/Li_2O$ mixture, in coincidence with the phenomenon reported in our previous work.[9] All these results demonstrate that H_2 annealing plays a significant role in enabling the high power densities from conversion reactions of the iron oxide/SWNT hybrid films as anodes for lithium-ion batteries.

To understand the electrochemical kinetics with respect to the enhancement of the rate capability, we employed electrochemical impedance spectroscopy (EIS) and the galvanostatic intermittent titration technique (GITT), which combines the transient and steady-state measurements to determine the Li^+ chemical diffusion coefficient, to compare the variation of kinetic parameters of the two samples before and after H_2 treatment. The EIS results are presented in Figure 6a with the inset equivalent circuit used to fit the data. The Nyquist plots show a typical Randles-model behavior,[19] which consists of a semicircle at high-to-middle frequency (100 kHz to 1 Hz) and a linear Warburg tail at low frequency (<1 Hz). In the corresponding equivalent circuit, R_s represents the series resistance of the electrodes, electrolyte, and the current collectors; R_{ct} is the charge-transfer resistance between electrode/electrolyte interface; CPE is the constant phase element; and W represents the Warburg impedance associated with the diffusion of the lithium ions. These parameters are calculated and presented in Table 1, where all the resistances are decreased after H_2 treatment. The lower series resistance of the film AH is benefitted from the high conductivity of Fe_3O_4. The nearly 50% drop of the charge-transfer resistance from 196.2 to 112.6 Ω after H_2 treatment confirms the improved conversion reaction kinetics determined by the charge-transfer process.[20] Most importantly, the H_2 annealing causes W to sharply decrease to 14.93 Ω compared to the original 96.83 Ω for the pure α-Fe_2O_3/SWNT hybrid films. This appreciable change is vital to facilitate the lithium diffusion and enhances the high-rate performance.

Table 1. Fitting Parameters of the Equivalent Circuit for EIS Data

	series resistance R_s (Ω)	charge-transfer resistance R_{ct} (Ω)	Warburg impedance W (Ω)
after H_2 treatment	6.23	112.6	14.93
before H_2 treatment	14.26	196.2	96.83

From the GITT curves of the two samples (Figure 6b) under the same conditions including the cutoff voltage, current density, and relaxation time, it is evident that regardless of the H_2 treatment, both possess a higher capacity of 1000 mA h g^{-1} than the steady-state capacity measured at 0.1 A g^{-1} due to the full relaxation of Li^+ diffusion. The plateau potential of the film AH is about 0.2 V higher than film BH, also lending evidence for the structure transformation of the nanocrystals, i.e. reduction of Fe_2O_3 to Fe_3O_4 during H_2 annealing. Another difference is that film AH has more GITT steps than film BH. In other words, the film AH proceeds to reach equilibrium faster for a single GITT step, which indicates higher transport kinetics after H_2 treatment than ever before.

Li^+ chemical diffusion coefficients can be calculated from the polarization curves extracted during the plateau according to the following equation[21]

$$D_{\mathrm{GITT}} = \frac{4}{\pi\tau}\left(\frac{m_b V_M}{M_b S}\right)^2\left(\frac{\Delta E_S}{\Delta E_t}\right)^2 \quad (1)$$

where τ is the constant current pulse time; m_b, M_b, and V_M are the mass, the molar mass, and the molar volume of the active electrode materials, respectively; S is the electrode area; ΔE_t is the total change of the cell voltage during the current pulse for the time t, neglecting the IR drop due to the current flux through the electrolyte and the interface; and ΔE_s is the change of the steady-state voltage of the cell for the step at plateau potential as illustrated and denoted in panels c and d in Figure 6. Considering the weight percentage of remaining Fe_2O_3 after H_2 treatment is only 7.5% of the iron oxide mixture, it can be deduced that most of Fe_2O_3 was converted to Fe_3O_4. Thus, for simplicity, we assume that after H_2 annealing, all the iron oxides become Fe_3O_4. The molar volume is calculated from eq 2 by using the crystal lattice parameters from the Rietveld fitting results of the XRD data in previous analysis

$$V_M = \frac{N_A V_{\mathrm{cell}}}{Z} \quad (2)$$

In this equation,[22] N_A is the Avogadro constant, V_{cell} is the unit-cell volume of the iron oxides, and Z is the number of formula units in the unit cell. The unit-cell information and the molar volumes of two iron oxides are listed in Table 2.

Table 2. Crystal Unit Cell Information and the Calculated Molar Volumes for the Two Iron Oxides

	V_{cell} (m^3)	Z	V_M (m^3 mol^{-1})
cubic Fe_3O_4	$a^3 = 5.90 \times 10^{-28}$	4	8.88×10^{-5}
rhombohedral Fe_2O_3	$a^2 c \sin 60° = 3.01 \times 10^{-28}$	6	3.02×10^{-5}

The polarization curves (Figure 6c, d) are representative of a single current pulse step at plateau potential during the charge and discharge processes for two samples, respectively. The $\Delta E_s/\Delta E_t$ items in eq 1 calculated from the polarization curves and M_b are summarized in Table 3. Because the variation of m_b and S could be neglected after H_2 treatment and τ remains the same, we can figure out the ratio of D_{GITT} for film AH and film BH in the equation as follows

Table 3. Results of $\Delta E_s/\Delta E_t$ and M_b Items from Calculation for the Two Iron Oxides

	$\Delta E_s/\Delta E_t$ on charge	$\Delta E_s/\Delta E_t$ on discharge	M_b (g mol^{-1})
cubic Fe_3O_4	0.82	0.17	251.53
rhombohedral Fe_2O_3	0.76	0.07	159.69

$$D_{GITT}^{AH}: D_{GITT}^{BH} = \left(\frac{V_M^{AH}}{V_M^{BH}}\right)^2 \left(\frac{M_b^{BH}}{V_b^{AH}}\right)^2 \left(\frac{\Delta E_S^{AH}}{\Delta E_t^{AH}}\right)^2 \left(\frac{\Delta E_S^{BH}}{\Delta E_t^{BH}}\right)^{-2} \quad (3)$$

where the items with the superscripts AH and BH refer to the samples after H_2 annealing and before H_2 annealing, respectively. By substituting the items in eq 3 with the data in Tables 2 and 3, the final $D_{GITT}^{AH}/D_{GITT}^{BH}$ upon charge and discharge at the plateau potential is calculated to be 1.80 and 10.30, respectively. The remarkable improvement of the Li^+ chemical diffusion coefficient, in particular to the discharge process, is consistent with the decreased Warburg impedance as emphasized in EIS analysis. Therefore, it is believed that the boost of D_{GITT} in particular during the discharge process contributes greatly to the excellent rate capability of iron oxides/SWNT hybrid films after H_2 treatment.

CONCLUSIONS

Iron oxide (Fe_2O_3 and Fe_3O_4)/SWNT hybrid films were synthesized by H_2 annealing of the pure α-Fe_2O_3/SWNT hybrid films. The materials exhibit an excellent cyclic stability and significantly enhanced rate capability with a high capacity of 786 mA h g^{-1} at the high current density of 4 A g^{-1}. The electrochemical kinetic analysis by GITT and EIS characterization demonstrates the superior conductivity of Fe_3O_4, facilitated charge-transfer process, and the improved Li^+ chemical diffusion coefficient resulted from H_2 annealing, which enables the high-rate capability of the iron oxide/SWNT hybrid films. This thermal reduction strategy proves to be an efficient fabrication procedure to boost the power density of rechargeable lithium batteries.

ASSOCIATED CONTENT

Supporting Information

Histogram information and inferometer image (PDF). This material is available free of charge via the Internet at http://pubs.acs.org.

AUTHOR INFORMATION

Corresponding Author

*E-mail: weib@udel.edu.

Notes

The authors declare no competing financial interest.

ACKNOWLEDGMENTS

We gratefully acknowledge the financial support from the U.S. National Science Foundation (NSF) under Contract 1067947.

REFERENCES

(1) Li, Y.; Tan, B.; Wu, Y. *Nano Lett.* **2008**, *8*, 265−270.
(2) Armstrong, A. R.; Armstrong, G.; Canales, J.; García, R.; Bruce, P. G. *Adv. Mater.* **2005**, *17*, 862−865.
(3) Taberna, P. L.; Mitra, S.; Poizot, P.; Simon, P.; Tarascon, J. M. *Nat. Mater.* **2006**, *5*, 567−573.
(4) Ohzuku, T.; Iwakoshi, Y.; Sawai, K. *J. Electrochem. Soc.* **1993**, *140*, 2490−2498.
(5) Sasidharan, M.; Gunawardhana, N.; Yoshio, M.; Nakashima, K. *Ionics* **2013**, *19*, 25−31.
(6) Hussain, S.; Hess, K.; Gearhart, J.; Geiss, K.; Schlager, J. *Toxicol. in Vitro* **2005**, *19*, 975−983.
(7) Zhu, X.; Zhu, Y.; Murali, S.; Stoller, M. D.; Ruoff, R. S. *ACS Nano* **2011**, *5*, 3333−3338.
(8) Ito, S.; Nakaoka, K.; Kawamura, M.; Ui, K.; Fujimoto, K.; Koura, N. *J. Power Sources* **2005**, *146*, 319−322.
(9) Cao, Z.; Wei, B. *J. Power Sources* **2013**, *241*, 330−340.
(10) Liu, D.; Liu, Y.; Pan, A.; Nagle, K. P.; Seidler, G. T.; Jeong, Y.-H.; Cao, G. *J. Phys. Chem. C* **2011**, *115*, 4959−4965.
(11) Jiao, F.; Harrison, A.; Jumas, J.-C.; Chadwick, A. V.; Kockelmann, W.; Bruce, P. G. *J. Am. Chem. Soc.* **2006**, *128*, 5468−5474.
(12) Coey, J.; Berkowitz, A.; Balcells, L.; Putris, F.; Parker, F. *Appl. Phys. Lett.* **1998**, *72*, 734−736.
(13) Zhu, H.; Wei, B. *Chem. Commun.* **2007**, *29*, 3042−3044.
(14) Toby, B. H. *J. Appl. Crystallogr.* **2001**, *34*, 210−213.
(15) Yamashita, T.; Hayes, P. *Appl. Surf. Sci.* **2008**, *254*, 2441−2449.
(16) de Faria, D. L. A.; Venâncio Silva, S.; de Oliveira, M. T. *J. Raman Spectrosc.* **1997**, *28*, 873−878.
(17) Aslan, S.; Loebick, C. Z.; Kang, S.; Elimelech, M.; Pfefferle, L. D.; Van Tassel, P. R. *Nanoscale* **2010**, *2*, 1789−1794.
(18) Maslar, J.; Hurst, W.; Bowers, W.; Hendricks, J.; Aquino, M. *J. Electrochem. Soc.* **2000**, *147*, 2532−2542.
(19) Randles, J. *Discuss. Faraday Soc.* **1947**, *1*, 11−19.
(20) Kang, Y.-M.; Song, M.-S.; Kim, J.-H.; Kim, H.-S.; Park, M.-S.; Lee, J.-Y.; Liu, H. K.; Dou, S. *Electrochim. Acta* **2005**, *50*, 3667−3673.
(21) Weppner, W.; Huggins, R. A. *J. Electrochem. Soc.* **1977**, *124*, 1569−1578.
(22) Mills, I.; Cvita, T.; Homann, K.; Kallay, N.; Kuchitsu, K. *Quantities, Units and Symbols in Physical Chemistry*, 2nd ed.; Blackwell Science: Oxford, U.K., 1993; p 41.